analytical chemistry

Article

Monitoring Changes in Biochemical and Biomechanical Properties of Collagenous Tissues Using Label-Free and Nondestructive Optical Imaging Techniques

Tanveer Ahmed Shaik,[⊥] João L. Lagarto,[⊥] Enrico Baria,[#] Melis Goktas,[#] Patrick Igoche Onoja, Kerstin G. Blank, Francesco S. Pavone, Jürgen Popp, Christoph Krafft,* and Riccardo Cicchi*

Cite This: https://dx.doi.org/10.1021/acs.analchem.0c04306

Read Online

ACCESS | Metrics & More | Article Recommendations | Supporting Information

ABSTRACT: We demonstrate the ability of nondestructive optical imaging techniques such as second-harmonic generation (SHG), two-photon fluorescence (TPF), fluorescence lifetime imaging (FLIM), and Raman spectroscopy (RS) to monitor biochemical and mechanical alterations in tissues upon collagen degradation. Decellularized equine pericardium (EP) was treated with 50 μg/mL bacterial collagenase at 37 °C for 8, 16, 24, and 32 h. The SHG ratio (defined as the normalized ratio between SHG and TPF signals) remained unchanged for untreated EP (stored in phosphate-buffered solution (PBS)), whereas treated EP showed a trend of a decreasing SHG ratio with increasing collagen degradation. In the fluorescence domain, treated EP experienced a red-shifted emission and the fluorescence lifetime had a trend of decreasing lifetime with increasing collagen digestion. RS monitors collagen degradation, the spectra had less intense Raman bands at 814, 852, 938, 1242, and 1270 cm^{-1}. Non-negative least-squares (NNLS) modeling quantifies collagen loss and relative increase of elastin. The Young's modulus, derived from atomic force microscope-based nanoindentation experiments, showed a rapid decrease within the first 8 h of collagen degradation, whereas more gradual changes were observed for optical modalities. We conclude that optical imaging techniques like SHG, RS, and FLIM can monitor collagen degradation in a label-free manner and coarsely access mechanical properties in a nondestructive manner.
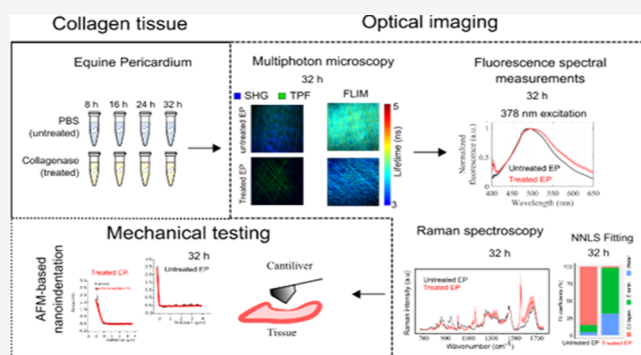
Collagen-based biomaterials are commonly used as scaffolds for tissue engineering and other biomedical applications.[1] Among all collagens, type I collagen is the most widely used biomaterial for biomedical applications due to its self-assembly, biocompatibility, biodegradability, and non-toxicity.[2] As the most abundant protein in the mammalian extracellular matrix (ECM), type I collagen is present in various tissues including muscles, cornea, bones, and teeth.[3,4] Type I collagen-based scaffolds used in the preparation of vascular grafts, xenografts, and tissue engineering applications are typically produced from bovine pericardium (BP), which consists of approximately 90% type I collagen (dry weight).[5] Similarly, equine pericardium (EP) has a well-organized type I collagen network, with equivalent mechanical and histological properties as BP. Common applications of EP include the manufacturing of heart valve prostheses,[6] dural repair,[7] scleroderma wound healing,[8] and diabetic foot wound healing.[9] Collagen scaffolds upon implantation are expected to lose mechanical strength during initial phases of remodeling,[10] which could be due to organized removal and digestion mediated by a different number of proteolytic enzymes belonging to the metalloproteinase family.[11−13] It is

therefore important to determine the mechanical properties of the tissue before implantation to ensure its long-term function and viability. Some applications, e.g., collagen graft development or regenerative applications could further benefit from a longitudinal and on-the-fly mechanical assessment. Typically, the mechanical properties of collagenous grafts are determined by uniaxial, multiaxial and circumferential tensile testing, and indentation.[14−17] While these tests guarantee excellent mechanical characterization, they often require a large amount of tissue to obtain reliable results, lack spatial information, are laborious and time consuming, and, most importantly, are destructive in nature,[18] which limits their applicability in longitudinal studies.[19] Optical imaging and spectroscopy have emerged as complementary tools for graft characterization due

ACS Publications

A

to their label-free and nondestructive nature. Optical measurements probe the interaction of light with absorbers and scatterers such as collagens, elastin, or lipids, and consequently offer means of probing the structural, chemical, and functional properties of a sample. Various optical modalities have been previously applied to probe the intrinsic properties of collagen-based constructs. For example, Raman spectroscopy (RS) has been employed to monitor chemical alterations in collagen-based scaffolds during cross-linking studies.[20−22] Similarly, two-photon fluorescence (TPF)[23,24] and fluorescence lifetime imaging microscopy (FLIM)[25] have been shown to report changes in the cross-linking environment,[26,27] collagen degradation,[28] and cell growth.[29,30] Second-harmonic generation (SHG) makes use of type I collagen noncentrosymmetric structural organization to report on ECM structure, including fiber density and orientation.[31] While these techniques alone can report on structural, chemical, or functional characteristics, it is common to employ a multimodal approach involving a combination of these modalities to harness complementary multidimensional information.

Our multimodal strategy employed RS and SHG to probe highly specific chemical and structural information and FLIM to probe functional information. We aimed to extensively characterize the optical signatures that accompany collagen degradation in EP and investigate how these correlate with changes in the mechanical properties of the tissue. In particular, we carried out measurements of SHG, TPF, FLIM, Raman spectra, and fluorescence emission spectra at 378 and 445 nm excitation at four different time points during *in vitro* degradation of EP using bacterial collagenase. To help establishing the correlation between optical and mechanical parameters, the mechanical assessment was carried using atomic force microscope (AFM)-based nanoindentation to determine the Young's modulus (YM).

Nanoindentation with a colloidal probe cantilever can evaluate the mechanical properties of the tissue without altering the fibrillar network of collagenous tissue.[32] When combined with optical modalities as FLIM,[33] RS,[34] or SHG,[35] such a multimodal approach has the ability to provide a complete characterization of the tissue, from biochemical to mechanical properties, in a nondestructive way.

◼ EXPERIMENTAL METHODS

Sample Preparation and Digestion. Decellularized EP tissue with approximate dimensions 3 cm × 5 cm was provided by Auto Tissue (Berlin, Germany). The tissue was initially washed in a phosphate-buffered solution (PBS) to remove any residues of the antibiotic solution in which it was stored. Next, the tissue was evenly divided into 24 pieces with approximately 1 cm × 0.7 cm dimensions each. Samples were equally separated into two groups: treated and untreated. A total of 12 samples were immersed in 50 μg/mL bacterial collagenase (C-0130, Merck KGaA, Darmstadt, Germany) to promote collagen digestion and ECM disruption. The remaining 12 samples were immersed in PBS and served as controls. Samples were incubated at 37 °C for 8, 16, 24, and 32 h (n = 3/time point and group) and then washed at room temperature with PBS. Samples were kept in PBS during the entire experiment, except when subject to microscopic or spectroscopic measurements.

Multiphoton Microscopy (SHG, TPF, and FLIM). Multiphoton imaging was realized in a custom-built laser-scanning microscope, which is described in detail else-

where.[36,37] In brief, excitation light was provided by an optical parametric oscillator (OPO) pumped by a frequency-doubled Yb-based fiber laser (Chameleon Discovery, Coherent, Santa Clara, CA) with a tunable output from 680 to 1300 nm, providing ∼100 fs optical pulses at a 80 MHz repetition rate. For measurements in this study, the laser was tuned to 770 nm. The laser beam was raster scanned using two galvanometric mirrors (Cambridge Technology, Bedford, MA) and focused onto the sample using a 40× dry objective lens (NA 0.95, WD 0.25 mm, Carl Zeiss Microscopy, Jena, Germany). The average power was measured to be approximately 20 mW immediately after the objective lens. Backward-emitted SHG and autofluorescence signals from the sample were collected by the same objective lens, reflected by a dichroic mirror (685DCXRU Chroma, Rockingham, VT) and directed to two photomultiplier tubes (PMT, H7422-40, Hamamatsu, Hamamatsu, Japan) for parallel and coregistered SHG and TPF imaging. A band-pass filter centered at 386 ± 11.5 nm (FF01-386/23-25, Semrock, Rochester, NY) was placed in the SHG optical path to selectively detect the second-harmonic signal. Two-photon excited autofluorescence detection was restricted to the band 510 ± 42 nm (FF01-510/84-25, Semrock). For simultaneous SHG and TPF imaging, each sample was mapped over three different locations, each consisting of twenty-five 150 μm × 150 μm tiles (512 × 512 pixels each), for a total field of view of 750 μm × 750 μm per location. The acquisition time for each tile was 5 s.

FLIM images were acquired independently and after SHG and TPF imaging. The optical path for FLIM measurements was similar to that described above, only using a photon-counting PMT (PMH-100, Becker & Hickl GmbH, Berlin, Germany) to detect the autofluorescence signals emanating from the sample within the 505 ± 59.5 nm band (FF01-505/119-25, Semrock). The PMT signal was routed to a time-correlated single-photon counting (TCSPC, SPC-150, Becker & Hickl) acquisition card that recorded the fluorescence intensity decay for each pixel. A set of three FLIM images were acquired with a field of view of 150 μm × 150 μm (128 × 128 pixels) from random locations within the regions mapped for SHG and TPF. The integration time for each FLIM image was 120 s.

Fluorescence Spectral Measurements. The setup for fluorescence spectral measurements was previously reported elsewhere.[38] Briefly, it consists of a fiber-based platform comprising two continuous-wave (CW) laser diodes emitting at 378 and 445 nm (LD = 378 and 445 nm—TEC42, Sacher Lasertechnik GmbH, Marburg, Germany) to excite tissue autofluorescence. The optical paths of both lasers are combined using a dichroic mirror (FF409-Di02, Semrock, Rochester, NY) and subsequently coupled to the central fiber of a custom-made bifurcated optical fiber bundle (EMVision LCC, Laxahatchee, FL). The fiber bundle consists of one central fiber used to deliver excitation light to the samples and 24 collection fibers arranged in a concentric ring around the delivery fiber at the distal end. All 25 fibers have a 100 μm core diameter and 0.22 NA. The autofluorescence signal is delivered to the detection system consisting of a microHR spectrometer (Horiba, Kyoto, Japan) fitted with a cooled charge-coupled device (CCD) detector (Syncerity, Horiba). At the detector end, 24 collection fibers are arranged in two lines to maximize transmission through the input slit of the detector. The detection system also includes a motorized filter wheel (Newport, Irvine, CA) equipped with two filters: a 402 nm

long-pass filter (03LWP402, CVI Melles Griot, Albuquerque, NM) to block 378 nm light and a 458 nm long-pass filter (LP02-458RS-25, Semrock) to block 445 nm light. Spectral measurements were performed sequentially for each excitation wavelength, with integration times of 50 ms (5 averages) for 378 nm, and 100 ms (5 averages) for 445 nm excitation. A total of five spectra were acquired for each sample. The position of the fiber was adjusted between acquisitions to ensure that different areas of the sample were measured. The fiber was maintained at approximately 2 mm from the sample during measurements.

Raman Spectroscopy. Raman spectra were acquired using a Kaiser RXN1 spectrometer (Ann Arbor, MI) equipped with an HoloProbe microscope. A 785 nm single-mode diode laser (Toptica Photonics AG, Graefelfing, Germany) was used to excite the tissue through a 20×/NA 1.0 water immersion objective (Nikon, Tokyo, Japan). The average power delivered to the sample was 130 mW. The Raman signal was collected in backscattering geometry and detected on a Peltier-cooled, back-illuminated, deep-depletion CCD chip (Andor, Belfast, Northern Ireland) after passing a holographic transmissive grating. The CCD was thermoelectrically cooled to −60 °C. The exposure time of Raman spectra acquisition was set to 4 s and 64 spectra were acquired from each sample.

Atomic Force Microscopy (AFM). AFM-based nano-indentation was carried out in a quantitative imaging (QI) mode. The EP samples were immobilized onto glass-bottom dishes (HBST-5030, Willco Wells, The Netherlands). For immobilization, Corning Cell-Tak Cell and Tissue Adhesive (Corning Inc. Life Sciences, Tewksbury, MA) was used. A hand-spreading method suggested by the supplier was performed as follows. The glass-bottom dishes were spread with 10 μL of Corning Cell-Tak in 5% acetic acid as a thin liquid film and then incubated with an open lid under the fume hood to let all liquid evaporate. As a result, an adhesive coating of Corning Cell-Tak was left on the glass surface. The EP samples were then placed on this thin adhesive film and incubated at room temperature for 30 min for the immobilization to take place. Once the immobilization was completed, the samples were rehydrated with PBS for 1 h prior to the measurement.

AFM-based QI was performed using a NanoWizard 3 AFM (JPK Instruments, Berlin, Germany). Silicon cantilevers (CONT-PS-D-5, NanoAndMore GmbH, Wetzlar, Germany) containing a polystyrene colloidal probe (diameter 10.8 μm) were used. The cantilevers possess a nominal spring constant of 0.02−0.77 N/m. Prior to imaging, calibration was performed using the contact-free thermal noise method in liquid. The actual spring constants ranged from 0.174 to 0.259 N/m. During imaging, the samples were kept hydrated in PBS, and all measurements were performed at room temperature. On all three samples, arrays of approach-retract curves were automatically collected in a QI mode with an applied load of 2 nN and a constant approach and retract speed of 50 μm/s. Stiffness maps were collected using a selected grid size of 10 × 10 pixels, distributed over an area of 100 × 100 μm scan size. In total, 15−30 different regions were probed on each sample.

Analysis of SHG and TPF Images. SHG and TPF images were initially treated to remove noise and the images were merged with blue and green channels, respectively. For each acquired image (n = 75 images per sample from n = 3 samples/group), a region of interest (ROI) with 100 × 100 pixels was selected and the corresponding mean SHG-to-TPF ratio was

calculated according to eq 1, where I_{SHG} is the mean SHG signal and I_{TPF} is the mean two-photon autofluorescence signal. SHG and TPF images were merged to demonstrate changes in SHG-to-TPF signals. All image processing was carried out using ImageJ 1.53a.[39]

$$\text{SHG ratio} = \frac{I_{SHG}}{I_{SHG} + I_{TPF}} \quad (1)$$

Analysis of FLIM. Fluorescence lifetime data were analyzed using a maximum likelihood-based estimator implemented in FLIMFit[40] to minimize the goodness of fit χ^2. Fluorescence intensity decays for each pixel were fitted to a biexponential decay model (eq 2)

$$F(t) = a_1\, e^{-t/\tau_1} + a_2\, e^{-t/\tau_2} + K \quad (2)$$

where a_1 and a_2 are pre-exponential factors, τ_1 and τ_2 are the individual fluorescence lifetimes of the fast and slow components of the fluorescence decay, respectively, and K is the constant background offset. The intensity weighted mean fluorescence lifetime τ_{mean} was determined as described in eq 3

$$\tau_{mean} = \frac{a_1\tau_1^2 + a_2\tau_2^2}{a_1\tau_1 + a_2\tau_2} \quad (3)$$

The model also included the detector after-pulsing probability, incomplete decay estimation, and the instrument response function (IRF), which was measured from the second-harmonic signal provided by a collagenous sample.

Analysis of Fluorescence Emission Spectra. Each measured fluorescence emission spectrum was normalized to its maximum intensity to minimize artifacts caused by uneven excitation-collection geometry from variable probe-to-target distances. The acquired spectra were corrected for filter transmission and spectral response of the CCD.

Analysis of Raman Spectra. Raman spectra were truncated in low and high wavenumber region and only the fingerprint region from 700 to 1800 cm^{-1} was used for analysis. Baseline correction was performed using an extended multi-plicative signal correction (EMSC) technique.[41] The EMSC matrix consists of a Raman spectrum from untreated and treated EP and each spectrum is considered as a pure component. The background components include five linear functions. The band at 1452 cm^{-1} with a high signal to noise ratio was used as an internal standard for normalizing the spectra. All Raman spectral preprocessing was performed using hyperSpec[42] and cbmodels[43] packages in R.

Raman spectra represent the macromolecular content of a compound as a linear combination of its biological constituents. We used a non-negative least-squares (NNLS) fitting for modeling the eq 4

$$X = cs + e \quad (4)$$

where X is the mean spectrum measured at various time points (8, 16, 24, and 32 h) and s is the spectral matrix of the individual biological compounds containing the Raman spectra of elastin (obtained from the porcine aorta), type I collagen (obtained from EP), and water. This spectral matrix was used as a reference to fit the Raman spectra of treated and untreated EP; c is the relative spectral contribution (fit coefficient) predicted by the model and e is the residual component of model fitting. NNLS was performed using nnls package[44] in R. The fit coefficients were normalized for every model by dividing the coefficient of each component to the summation
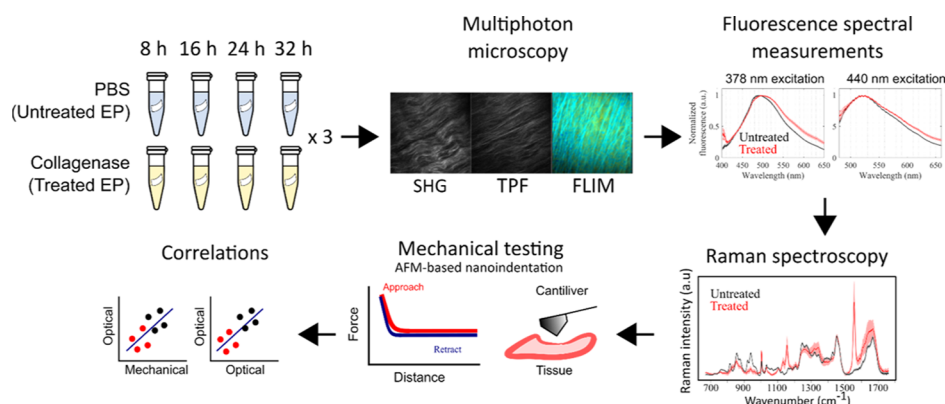
Figure 1. Experimental workflow depicting sample preparation, optical microscopic and spectroscopy measurements, mechanical examination through atomic force microscope (AFM)-based nanoindentation, and correlation analysis.
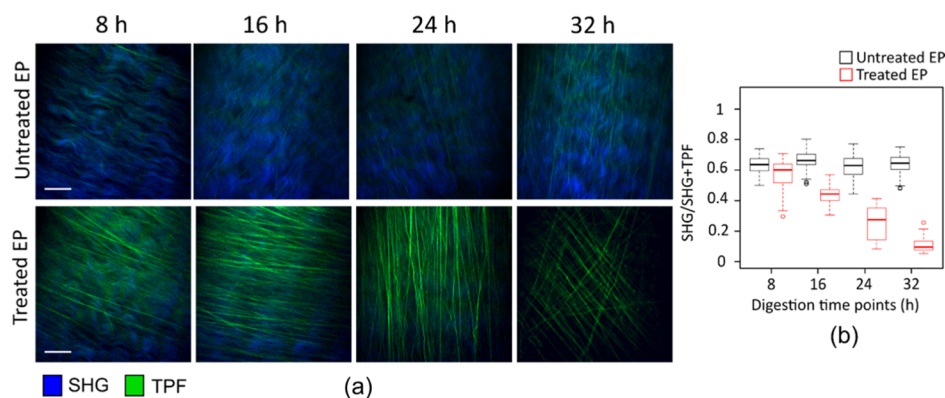
Figure 2. (a) Merged SHG (in blue) and TPF (in green) representative images of equine pericardium for untreated (top row) and treated (bottom row) samples at each time point. Scale bar = 20 μm. (b) Normalized SHG ratio (SHG/SHG+TPF) of n = 3 samples/group is plotted as a function of treatment time.

of all of the fit coefficients and expressed in the form of a percentage.

Analysis of AFM Nanoindentation. JPK SPM data processing software (JPK Instruments) was used for extracting the YM. The collected approach curves were batch analyzed using the Hertz−Sneddon fit function (spherical indenter) and a Poisson ratio of 0.5. For the samples treated with collagenase for 32 h, the fit was only applied up to an indentation depth of 0.3 μm. For these samples, a drastic decrease in the volume and thickness was observed. The Hertz model is only valid for small indentations (up to 5−10% of the sample thickness, approximately 0.2−0.5 μm for the treated 32 h sample), where the underlying glass substrate does not influence the calculated YM. For each sample, the obtained YM values were plotted into histograms using Igor Pro 7 (WaveMetrics Inc., Oregon). The histograms were fitted with Gaussian distribution to determine the most probable YM. In addition, the mean and the standard deviation (SD) were calculated for each distribution.

RESULTS AND DISCUSSION

Collagen Quantification Based on SHG. Treatment of EP with 50 μg/mL bacterial collagenase resulted in visible digestion of the samples from 8 to 32 h (Figure 1). Samples treated with bacterial collagenase became increasingly translucent and slimy with treatment time, suggesting a decrease in optical absorption and loss of the structure as a result of collagen degradation and removal from tissue. No changes were visible in untreated samples (immersed in PBS) over time. EP has a well-organized ECM that is primarily composed of collagen type I and, in lesser amounts, elastin. Being highly noncentrosymmetric, collagen yielded a strong SHG signal in all untreated samples (see Figure 2a, top row). In particular, our data show that collagen fibers are arranged in a wave-like structure (in blue) and without a particular orientation. In contrast, elastin fibers are well-visible and dominate the two-photon excited autofluorescence signal (in green). Elastin fibers appear to be more rectilinear and have the same general orientation as fibrillar collagen in untreated samples. The ratio of SHG to autofluorescence signal remained constant over time for untreated samples (see Figure 2b, in black). Treatment with bacterial collagenase resulted in a consistent decrease of the SHG signal over time, as a consequence of collagen cleavage and loss of its noncentrosymmetric properties. This is evident in the merged SHG and TPF images, see Figure 2a bottom row.

In contrast, treatment with bacterial collagenase did not seem to affect elastin autofluorescence properties and, therefore, we measured a consistent decrease of the SHG signal with respect to the total measured signal (Figure 2b). Indeed, the absolute autofluorescence intensity was higher in treated samples compared to untreated samples (data not shown), which is possibly related to the decrease in scattering in treated samples due to the loss of collagen, with a corresponding increase in optical penetration. Therefore, the decrease in the SHG ratio over time can be interpreted as a
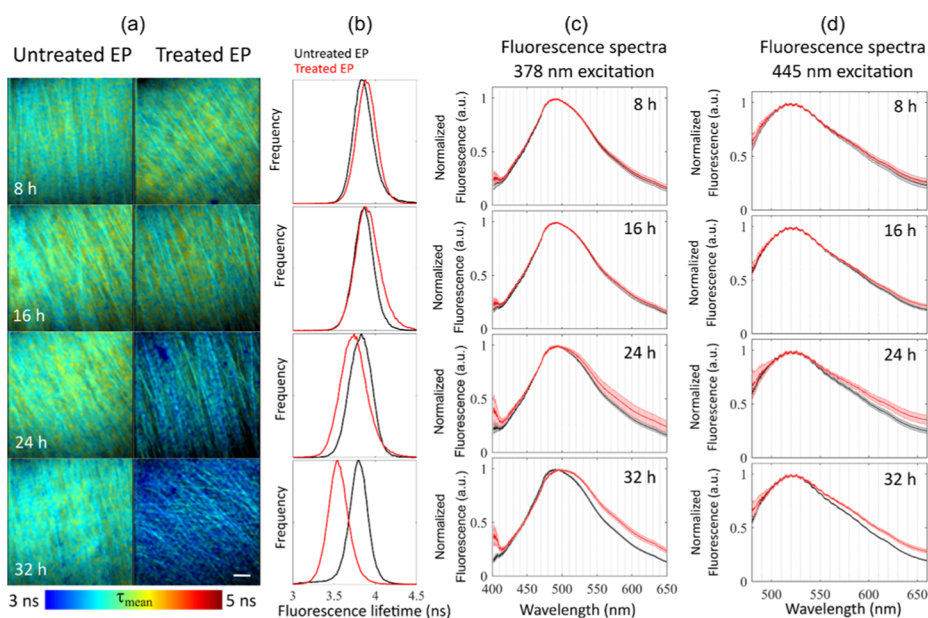
Figure 3. (a) Representative fluorescence lifetime maps of untreated and treated samples. Scale bar = 20 μm. (b) Distribution of fluorescence lifetimes for all samples, showing a decrease in mean fluorescence lifetime of treated samples with digestion time relative to untreated samples. Fluorescence emissions spectra excited at (c) 378 nm and (d) 445 nm, suggesting a red shift in the fluorescence emission of treated samples (in red) relative to untreated samples (in black). Solid lines and corresponding shaded regions indicate mean $\pm$ SD (n = 3 samples/group), respectively.
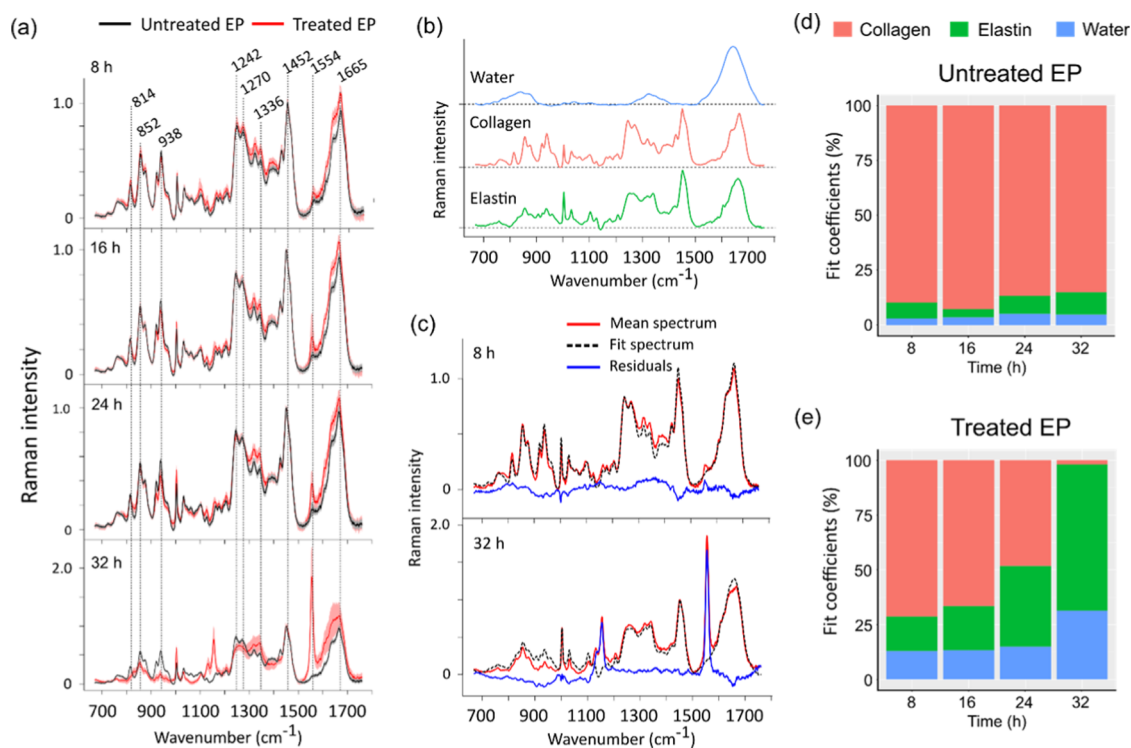

Figure 4. (a) Mean and standard deviation of normalized Raman spectra of untreated (black) and digested (red) samples for n = 3 samples of 8, 16, 24, and 32 h time points. (b) Pure components spectra of NNLS model fitting and (c) NNLS fitting results at 8 h and 32 h digestion time points (using n = 3/group). Fit coefficients of collagen, elastin, and water in percentages for (d) untreated EP and (e) digested EP.

combination of collagen depletion and the increase of the measured elastin signal.

Fluorescence Lifetime and Spectral Changes upon Collagen Degradation. To investigate functional changes that occur in EP during collagen digestion, we carried out two-photon-excited FLIM measurements. For untreated samples,

we measured a mean fluorescence lifetime of 3.83 $\pm$ 0.06 ns (mean $\pm$ SD) of all samples (see Figure 3a,b). We note that, for untreated samples, the fluorescence lifetime appears to decrease slightly though not significantly over time (from 3.87 $\pm$ 0.05 to 3.78 $\pm$ 0.05 ns, n = 3 samples), which may be a result of the release of ECM components such as proteoglycans

without proteolytic degradation.[45,46] A decrease in fluorescence lifetime was more pronounced in samples treated with bacterial collagenase. This is evident in Figure 3b (red curves), where we observe a shift in mean fluorescence lifetime from 3.89 ± 0.02 ns at 8 h to 3.56 ± 0.04 ns at 32 h treatment. This decrease is consistent with the previous observation by Li et al.[47] using a fiber-based approach. Given the decrease in the collagen content with digestion time measured by SHG, the decrease in fluorescence lifetime with digestion probably reflects an increase in the relative contribution of elastin fibers to the autofluorescence signal. This result further suggests that elastin yields a shorter lifetime compared to type I collagen.

To further understand changes in the optical signatures of EP upon digestion, we carried out fluorescence spectral measurements at wavelengths of interest: 378 and 445 nm. The fluorescence excitation and emission characteristics of both collagen and elastin are known to be complex, owing to the multitude of cross-links that can be excited and contribute to the autofluorescence signal. While both collagen and elastin are well excited at 378 nm, collagen fluorescence peaks at ~460 nm, while elastin emanates strong fluorescence at wavelengths longer than 500 nm. Results in Figure 3c show a gradual red shift in the normalized fluorescence emission of treated samples (red curves) with digestion time, which suggests an increasing contribution of elastin autofluorescence with a concomitant decrease in the collagen signal. These data further support previous observations from multiphoton and FLIM measurements. We also note that the absolute fluorescence intensity of treated samples decreased with digestion, as a consequence of collagen cleavage and removal, and decrease optical absorption. In the spectra, this is evidenced by the relative increase of laser bleed-through at 24 and 32 h (see the spectral shape between 400 and 410 nm). The spectral profile of untreated samples excited at 378 nm (Figure 3c, black curves) remained relatively unaltered with digestion, peaking at around 490 nm. In contrast to the spectral profiles measured at 378 nm excitation, at 445 nm excitation (Figure 3d), we measured more subtle differences between untreated and treated samples. Changes were most visible at longer wavelengths (>550 nm), possibly because elastin emits more fluorescence in this range compared to collagen.

Biochemical Quantification of Collagen Degradation Based on Raman Spectra. The Raman spectra of EP samples following 8, 16, 24, and 32 h of treatment are shown in Figure 4a. Our Raman data of untreated and treated EP samples include spectral features consistent with the presence of proline (814 cm^{-1}), hydroxyproline (852 cm^{-1}), C−C$_\alpha$ stretch (938 cm^{-1}), phenylalanine (1004 cm^{-1}), amide III (1242 and 1270 cm^{-1}), CH$_2$/ CH$_3$ collagen and elastin (1452 cm^{-1}), and amide I (1666 cm^{-1}),[21,22,48] which are characteristic of Raman spectra of collagen, thus confirming that type I collagen is the major component of EP as previously found in the bovine pericardium.[21,22] The Raman spectra of untreated EP remained relatively unaltered for all time points (see Figure 4a, spectra in black). For 8 h of digestion, we found similar spectral features between untreated and treated samples. For digested samples (Figure 4a, spectra in red), the Raman spectral intensity decreased at proline, hydroxyproline, C−C$_\alpha$ stretch, and amide I regions with digestion time. In particular, the Raman spectral features of proline, C−C$_\alpha$ stretch, and amide III that are characteristic of type I collagen were absent at 32 h of digestion, suggesting strong depletion of the collagen

content. Further, new Raman bands appeared at 1336 cm^{-1}, which are suggestive of the presence of elastin.[49] In addition to the spectral features of elastin, strong Raman bands were observed at 1156 and 1554 cm^{-1} at 32 h of digestion. We believe these bands are not resultant of digestion since they were also observed in native EP tissue (data not shown). The tentative assignment for these bands could be a conjugated pi-electron system detected in carotenoid-like pigments having different carbon chain lengths[50,51] or nitrogen-containing carbon chain-like syringaldazine, as suggested by Know-It-All database (Wiley).

To quantify collagen loss and detect the presence of elastin in EP, we employed an NNLS fitting technique to fit the measured EP Raman spectra. Since EP is primarily composed of collagen, elastin, and water, the pure Raman spectra of these components (see Figure 4b) were used as fitting components, and the resulting fit coefficients provided a quantitative assessment of each samples' composition. Figure 4c shows the model fitting results for 8 h and 32 h digestion time points with mean, fitted, and the residual spectrum. Residuals are small and mainly related to background fluctuations except for the not yet identified conjugated pi-electron system. Table S1 (Supporting Information) shows the average fit coefficients of $n = 3$ samples/group at all time points. Minimal variations were observed in the coefficients of untreated EP for the different time points (see Figure 4d). We noted a small decrease in the collagen content with time (from 89.80% at 8 h to 85.21% at 32 h) with a concomitant increase in elastin and water contribution. This result is consistent with our fluorescence lifetime measurements of untreated samples where we measured a slight decrease in fluorescence lifetime over time (see Figure 3b). Overall, for untreated samples, the average coefficients were calculated to be 88.6% for collagen, 7.27% for elastin, and 4% for water, which can be correlated with the proportion of these components in EP.[52,53]

Fit coefficients of collagen, elastin, and water for treated samples are shown in Figure 4e. For treated EP, we measured a trend of decreasing collagen content, from 71.4% at 8 h to 1.9% after 32 h. This decrease was necessarily accompanied by a relative increase in elastin and water contribution. For elastin, we measured an increase from 15.6% at 8 h to 66.6% after 32 h. Similarly, the water fit coefficient increased from 12.8% at 8 h to 31.3% after 32 h. Detailed fit coefficients for untreated and treated EP are summarized in Table S1 (Supporting Information).

Relationship between Optical Parameters and YM. AFM-based nanoindentation was performed on untreated and treated EP to determine the YM of the tissue. For the untreated EP samples, no clear change of YM was visible with increasing incubation time and the mean sample YM ranged from 3.03 to 8.64 kPa (SD = 1.86 kPa across all incubation times). Importantly, of all samples investigated, untreated EP with an intact collagen network was found to have the highest YM. With treatment, the mean sample YM decreased to 1.83 kPa after 8 h of incubation and 0.55 kPa after 16 h. The largest relative decrease in YM was thus already observed after the first 8 h of treatment. After 16 h, a plateau was approached and the YM did not decrease much further at the 24 h and 32 h time points with values of 0.49 and 0.43 kPa, respectively (refer to the Supporting Information, Tables S2 and S3, Figures S1−S4 for detailed information). In contrast, severe alterations of the collagen content were only observed after 24 h and 32 h of treatment in our optical measurements.
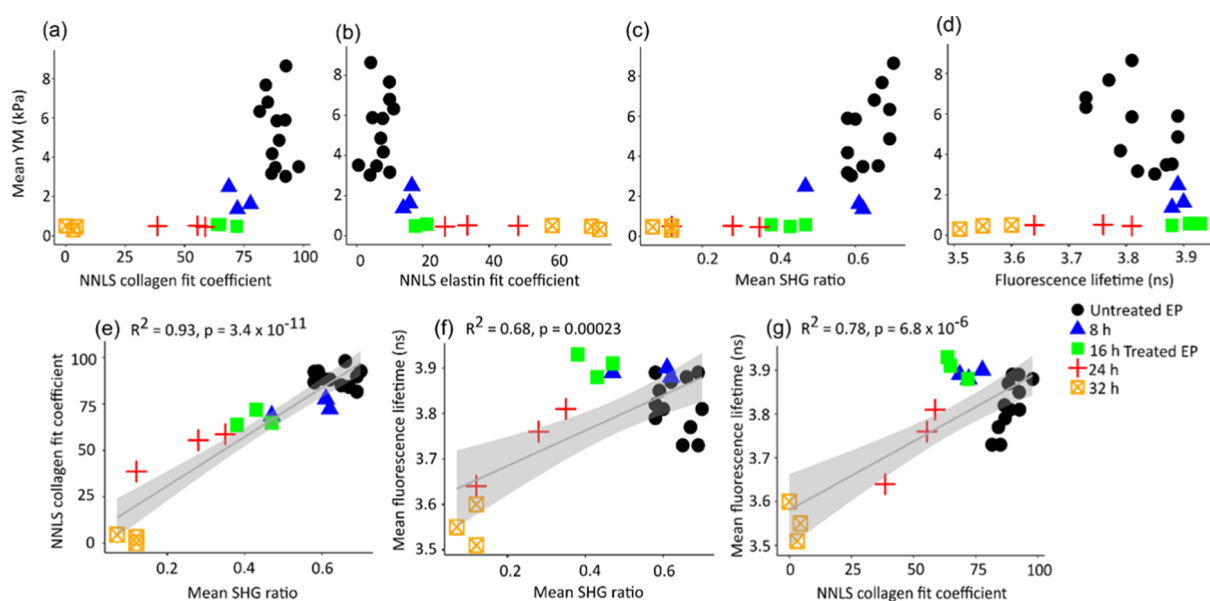
Figure 5. Scatterplots of the (a) RS NNLS collagen fit coefficient vs YM, (b) RS NNLS elastin fit coefficient vs YM, (c) SHG ratio vs YM, and (d) fluorescence lifetime vs YM. Interoptical correlation. Pearson's correlation of the (e) SHG ratio vs NNLS collagen fit coefficient, (f) SHG ratio vs fluorescence lifetime, and (g) NNLS collagen fit coefficient vs fluorescence lifetime (shaded region represents 95% confidence intervals) (sample wise mean is calculated for NNLS collagen and elastin fit coefficients, SHG ratio, fluorescence lifetime time, and YM).

Our data do not suggest a strong correlation between optical parameters and Young's modulus (see Figure 5). It is, however, possible to identify trends in the data. For example, the YM decreases with the NNLS collagen fit coefficient and the SHG signal (see Figure 5a,c). These optical parameters are specific to collagen and therefore are indicative of collagen-related changes occurring upon degradation. Quantitative assessment based on optical parameters of RS and SHG shows that a lower amount of collagen leads to a reduced YM, which is a measure of tissue stiffness. Like the NNLS collagen fit coefficient and SHG signal, the YM decreased with fluorescence lifetime (Figure 5d). Conversely, a negative trend was observed for the NNLS fit coefficient of elastin and YM modulus (Figure 5b), which is a direct result of the apparent increase in the elastin content relative to the remaining amount of collagen. Assuming that the absolute elastin content remains constant during collagen degradation, we hypothesize that the presence of elastin does not contribute to the stiffness of the material. In general, our data suggest that optical parameters show a gradual decrease or increase upon collagen degradation, whereas the largest changes in YM already took place before the 8 h time point with little further change after 16 h. This result suggest that the collagen network loses tension after initial cleavage of a small number of collagen fibers. To understand this process in more detail, mechanical measurements at shorter incubation times are interesting to perform in future experiments.

Optical imaging modalities SHG, RS, and FLIM provide complementary structural and biochemical information. The complementarity between RS and SHG was evaluated by performing Pearson's correlation for the mean SHG ratio vs NNLS collagen fit coefficient ($R^2 = 0.93$, $p = 3.4 \times 10^{-11}$) (Figure 5e). Both RS and SHG are very strongly correlated because these imaging modalities probe biochemical information with high specificity. Similarly, a decent correlation can be established between the SHG ratio vs fluorescence lifetime ($R^2 = 0.68$, $p = 0.0023$) (Figure 5f), and NNLS collagen fit

coefficient vs fluorescence lifetime ($R^2 = 0.78$, $p = 6.2 \times 10^{-6}$) (Figure 5g). One of the reasons for moderate correlations of FLIM vs RS and SHG is that FLIM probes functional changes that could be beyond the changes observed by RS and SHG. However, the biochemical information of SHG and RS can be used to complement and enhance the biochemical specificity of imaging modalities like FLIM, which suffers from moderate biochemical specificity.

■ CONCLUSIONS

In this study, we demonstrated that optical measurements provide an indirect assessment of chemical, structural, and functional alterations in collagenous tissues that can be coarsely correlated to changes in the mechanical properties in a nondestructive and label-free manner.

Treatment of EP with bacterial collagenase resulted in digestion and removal of type I collagen, which strongly affected the tissue optical properties of SHG, FLIM, and RS. In particular, changes in the tissue ECM were accompanied by alterations in the mechanical properties measured by AFM-based nanoindentation, and our results suggest that both SHG and Raman NNLS-derived parameters (relative proportions of collagen and elastin) have the potential to coarsely monitor such alterations.

As for FLIM, our results indicate that the fluorescence lifetime of EP decreases with collagen digestion, which is consistent with previous observations. Yet, we could not establish a direct correlation between FLIM data and YM derived from AFM-based nanoindentation.

Optical imaging modalities can provide complementary multidimensional collagen fiber-level information that can be combined with AFM for characterization of the structural, biochemical, and mechanical properties of the tissue with high specificity in a nondestructive and label-free manner. These optical techniques can be implemented through a optical fiber-based technology.

In conclusion, SHG, FLIM, and RS can address the unmet needs of tissue engineering and regenerative medicine applications. Such multimodal imaging approach can create a platform to access biochemical, structural, and mechanical information in a nondestructive and label-free manner.

■ ASSOCIATED CONTENT

Ⓢ Supporting Information

The Supporting Information is available free of charge at https://pubs.acs.org/doi/10.1021/acs.analchem.0c04306.

> Representative nanoindentation results and YM histograms for each sample, the table of mean Young's modulus, and NNLS fit coefficients of Raman spectra of untreated and treated EP (PDF)

■ AUTHOR INFORMATION

Corresponding Authors

Christoph Krafft − *Leibniz Institute of Photonic Technology, 07745 Jena, Germany*; Email: Christoph.krafft@leibniz-ipht.de

Riccardo Cicchi − *National Institute of Optics (INO), National Research Council (CNR), 50125 Florence, Italy; European Laboratory for Non-Linear Spectroscopy (LENS), University of Florence, 50019 Sesto Fiorentino, Italy*; ⓞ orcid.org/0000-0002-2583-6694; Email: riccardo.cicchi@ino.cnr.it, rcicchi@lens.unifi.it

Authors

Tanveer Ahmed Shaik − *Leibniz Institute of Photonic Technology, 07745 Jena, Germany*; ⓞ orcid.org/0000-0002-3235-5709

João L. Lagarto − *National Institute of Optics (INO), National Research Council (CNR), 50125 Florence, Italy; European Laboratory for Non-Linear Spectroscopy (LENS), University of Florence, 50019 Sesto Fiorentino, Italy*

Enrico Baria − *National Institute of Optics (INO), National Research Council (CNR), 50125 Florence, Italy; European Laboratory for Non-Linear Spectroscopy (LENS), University of Florence, 50019 Sesto Fiorentino, Italy*

Melis Goktas − *Mechano(bio)chemistry, Max Planck Institute of Colloids and Interfaces, 14476 Potsdam, Germany*

Patrick Igoche Onoja − *Leibniz Institute of Photonic Technology, 07745 Jena, Germany*

Kerstin G. Blank − *Mechano(bio)chemistry, Max Planck Institute of Colloids and Interfaces, 14476 Potsdam, Germany*; ⓞ orcid.org/0000-0001-5410-6984

Francesco S. Pavone − *National Institute of Optics (INO), National Research Council (CNR), 50125 Florence, Italy; European Laboratory for Non-Linear Spectroscopy (LENS), University of Florence, 50019 Sesto Fiorentino, Italy*

Jürgen Popp − *Leibniz Institute of Photonic Technology, 07745 Jena, Germany; Institute of Physical Chemistry, Friedrich Schiller University, 07743 Jena, Germany; Abbe Center of Photonics, Friedrich Schiller University, 07745 Jena, Germany*; ⓞ orcid.org/0000-0003-4257-593X

Complete contact information is available at:
https://pubs.acs.org/10.1021/acs.analchem.0c04306

Author Contributions

⊥T.A.S. and J.L. contributed equally as first authors.

Author Contributions

#E.B. and M.G. contributed equally as second authors. T.A.S., C.K., and R.C. proposed the idea and methodology. T.A.S. performed data analysis (SHG, TPF, and RS) and pilot measurements of the study. T.S. and J.L.L. wrote the manuscript. J.L.L. prepared the samples and performed SHG, TPF, FLIM, and fluorescence spectral measurements. J.L.L performed data analysis (FLIM and fluorescence spectroscopy). E.B. performed SHG, TPF, FLIM, and fluorescence spectral measurements. M.G. performed AFM-based nanoindentation and related data processing. P.I.O. collected Raman spectra. C.K. provided inputs on Raman spectral data processing. K.B provided inputs on AFM-based nanoindentation. M.G., C.K., K.B., F.P., J.P., and R.C. participated in the layout and manuscript preparation.

Notes

The authors declare no competing financial interest.

■ ACKNOWLEDGMENTS

■ REFERENCES

(1) Parenteau-Bareil, R.; Gauvin, R.; Berthod, F. *Materials* **2010**, *3*, 1863−1887.

(2) Hasirci, V.; Vrana, E.; Zorlutuna, P.; Ndreu, A.; Yilgor, P.; Basmanav, F. B.; Aydin, E. *J. Biomater. Sci. Polym. Ed.* **2006**, *17*, 1241−1268.

(3) Fratzl, P. *Collagen Struct. Mech.* **2008**, 1−13.

(4) Shoulders, M. D.; Raines, R. T. *Annu. Rev. Biochem.* **2009**, *78*, 929−958.

(5) Schoen, F. J.; Tsao, J. W.; Levy, R. J. *Am J Pathol* **1986**, *123*, 134−145.

(6) Rassoli, A.; Fatouraee, N.; Guidoin, R.; Zhang, Z. *Artif. Organs* **2020**, *44*, 278−287.

(7) Centonze, R.; Agostini, E.; Massaccesi, S.; Toninelli, S.; Morabito, L. *Asian J. Neurosurg.* **2016**, *11*, 201.

(8) Mulder, G.; Lee, D. K. *Wounds* **2009**, *21*, 297−301.

(9) Fleischli, J. G.; Laughlin, T. J.; Fleischli, J. W. *J. Am. Podiatr. Med. Assoc.* **2009**, *99*, 301−305.

(10) Weiler, A.; Hoffmann, R.; Stähelin, A.; Helling, H. J.; Südkamp, N. *Arthroscopy* **2000**, *16*, 305−321.

(11) Nagano, J.; Shino, K.; Maeda, A.; Nakata, K.; Horibe, S. *Arch. Orthop. Trauma Surg.* **1996**, *115*, 10−16.

(12) Lo, I. K. Y.; Marchuk, L. L.; Hollinshead, R.; Hart, D. A.; Frank, C. B. *Am. J. Sports Med.* **2004**, *32*, 1223−1229.

(13) Yoshihara, Y.; Hamada, K.; Nakajima, T.; Fujikawa, K.; Fukuda, H. *J. Orthop. Res.* **2001**, *19*, 573−579.

(14) Elliott, M. B.; Ginn, B.; Fukunishi, T.; Bedja, D.; Suresh, A.; Chen, T.; Inoue, T.; Dietz, H. C.; Santhanam, L.; Mao, H.-Q.; Hibino,

N.; Gerecht, S. *Proc. Natl. Acad. Sci. U.S.A.* **2019**, *116*, 12710 LP–12712719.

(15) Mauri, A.; Zeisberger, S. M.; Hoerstrup, S. P.; Mazza, E. *Tissue Eng., Part A* **2013**, *19*, 583–592.

(16) Li, X.; Guo, Y.; Ziegler, K.; Model, L.; Eghbalieh, S.; Brenes, R.; Kim, S.; Shu, C.; Dardik, A. *Ann. Vasc. Surg.* **2011**, *25*, 561–568.

(17) McKee, C. T.; Last, J. A.; Russell, P.; Murphy, C. J. *Tissue Eng., Part B. Rev.* **2011**, *17*, 155–164.

(18) Griffin, M.; Premakumar, Y.; Seifalian, A.; Butler, P. E.; Szarko, M. *J. Vis. Exp.* **2016**, 54872.

(19) Frese, J.; Morgenroth, A.; Mertens, M.; Koch, S.; Rongen, L.; Vogg, A.; Zlatopolskiy, B.; Neumaier, B.; Gesche, V.; Lammers, T.; Schmitz-Rode, T.; Mela, P.; Jockenhoevel, S.; Mottaghy, F.; Kiessling, F. *Biomed. Tech.* **2013**, *59*, 1–11.

(20) Ember, K. J. I.; Hoeve, M. A.; McAughtrie, S. L.; Bergholt, M. S.; Dwyer, B. J.; Stevens, M. M.; Faulds, K.; Forbes, S. J.; Campbell, C. J. *npj Regen. Med.* **2017**, *2*, No. 12.

(21) Shaik, T. A.; Alfonso-García, A.; Zhou, X.; Arnold, K. M.; Haudenschild, A. K.; Krafft, C.; G Griffiths, L.; Popp, J.; Marcu, L. *Anal. Chem.* **2020**, *92*, 10659–10667.

(22) Shaik, T. A.; Alfonso-Garcia, A.; Richter, M.; Korinth, F.; Krafft, C.; Marcu, L.; Popp, J. *Molecules* **2020**, *25*, 3857.

(23) Sun, Y.; Tan, H.-Y.; Lin, S.-J.; Lee, H.-S.; Lin, T.-Y.; Jee, S.-H.; Young, T.-H.; Lo, W.; Chen, W.-L.; Dong, C.-Y. *Microsc. Res. Tech.* **2008**, *71*, 140–145.

(24) Whited, B. M.; Hofmann, M. C.; Lu, P.; Xu, Y.; Rylander, C. G.; Wang, G.; Sapoznik, E.; Criswell, T.; Lee, S. J.; Soker, S.; Rylander, M. N. *PLoS One* **2013**, *8*, e61275–e61275.

(25) Binder, B. Y.; Leach, J.; Marcu, L. Fluorescence Lifetime Imaging Applications in Tissue Engineering. In *Fluorescence Lifetime Spectroscopy and Imaging: Principles and Applications in Biomedical Diagnostics*; CRC Press: 2014; pp 449–458.

(26) Batista, A.; Breunig, H. G.; Hager, T.; Seitz, B.; König, K. *Sci. Rep.* **2019**, *9*, No. 10241.

(27) Marturano, J. E.; Xylas, J. F.; Sridharan, G. V.; Georgakoudi, I.; Kuo, C. K. *Acta Biomater.* **2014**, *10*, 1370–1379.

(28) Manning, H. B.; Nickdel, M. B.; Yamamoto, K.; Lagarto, J. L.; Kelly, D. J.; Talbot, C. B.; Kennedy, G.; Dudhia, J.; Lever, J.; Dunsby, C.; French, P.; Itoh, Y. *Matrix Biol.* **2013**, *32*, 32–38.

(29) Alfonso-Garcia, A.; Shklover, J.; Sherlock, B. E.; Panitch, A.; Griffiths, L. G.; Marcu, L. *J. Biophotonics* **2018**, *11*, No. e201700391.

(30) Meleshina, A. V.; Dudenkova, V. V.; Bystrova, A. S.; Kuznetsova, D. S.; Shirmanova, M. V.; Zagaynova, E. V. *Stem Cell Res. Ther.* **2017**, *8*, No. 15.

(31) Fuentes-Corona, C. G.; Licea-Rodriguez, J.; Younger, R.; Rangel-Rojo, R.; Potma, E. O.; Rocha-Mendoza, I. *Biomed. Opt. Express* **2019**, *10*, 6449–6461.

(32) Stylianou, A. *J. Nanomater.* **2017**, *2017*, No. 9234627.

(33) Micic, M.; Hu, D.; Suh, Y. D.; Newton, G.; Romine, M.; Lu, H. P. *Colloids Surf., B* **2004**, *34*, 205–212.

(34) Janko, M.; Davydovskaya, P.; Bauer, M.; Zink, A.; Stark, R. W. *Opt. Lett.* **2010**, *35*, 2765–2767.

(35) Quigley, A. S.; Bancelin, S.; Deska-Gauthier, D.; Légaré, F.; Veres, S. P.; Kreplak, L. *Sci. Data* **2018**, *5*, No. 180229.

(36) Mercatelli, R.; Mattana, S.; Capozzoli, L.; Ratto, F.; Rossi, F.; Pini, R.; Fioretto, D.; Pavone, F. S.; Caponi, S.; Cicchi, R. *Commun. Biol.* **2019**, *2*, No. 117.

(37) Marchetti, M.; Baria, E.; Cicchi, R.; Pavone, F. S. *Methods Protoc.* **2019**, *2*, 51.

(38) Anand, S.; Cicchi, R.; Giordano, F.; Conti, V.; Buccoliero, A. M.; Guerrini, R.; Pavone, F. S. *J. Biophotonics* **2017**, *10*, 896–904.

(39) Schindelin, J.; Arganda-Carreras, I.; Frise, E.; Kaynig, V.; Longair, M.; Pietzsch, T.; Preibisch, S.; Rueden, C.; Saalfeld, S.; Schmid, B.; Tinevez, J.-Y. Y.; White, D. J.; Hartenstein, V.; Eliceiri, K.; Tomancak, P.; Cardona, A. *Nat. Methods* **2012**, *9*, 676–682.

(40) Warren, S. C.; Margineanu, A.; Alibhai, D.; Kelly, D. J.; Talbot, C.; Alexandrov, Y.; Munro, I.; Katan, M.; Dunsby, C.; French, P. M. W. *PLoS One* **2013**, *8*, No. e70687.

(41) Skogholt, J.; Liland, K. H.; Indahl, U. G. *J. Raman Spectrosc.* **2019**, *50*, 407–417.

(42) Beleites, C.; Sergo, V. *HyperSpec: A Package to Handle Hyperspectral Data Sets in R*.2018.

(43) Beleites, C.. *"cbmodels: Collection of 'Combined' Models: PCA-LDA, PLS-LDA, PLS-LR as Well as EMSC"*, R Package Version 0.5-20150729; 2015.

(44) Mullen, K. M.; van Stokkum, I. H. M.. *Nnls: The Lawson-Hanson Algorithm for Non-Negative Least Squares (NNLS)*; 2012.

(45) Yansen, E. S.; Ignat'eva, N.; Averkiev, S. V.; Shekhter, A.; Lunin, V. V.; Sobol, E. *Laser Phys.* **2005**, *15*, 1660–1663.

(46) Lagarto, J. L.; Nickdel, M. B.; Kelly, D. J.; Price, A.; Nanchahal, J.; Dunsby, C.; French, P.; Itoh, Y. *Sci. Rep.* **2020**, *10*, No. 2154.

(47) Li, C.; Shklover, J.; Parvizi, M.; Sherlock, B. E.; Alfonso Garcia, A.; Haudenschild, A. K.; Griffiths, L. G.; Marcu, L. *Ann. Biomed. Eng.* **2018**, *46*, 1870–1881.

(48) Krafft, C.; Codrich, D.; Pelizzo, G.; Sergo, V. *J. Biophotonics* **2008**, *1*, 154–169.

(49) Frushour, B. G.; Koenig, J. L. *Biopolymers* **1975**, *14*, 379–391.

(50) Jehlička, J.; Edwards, H. G. M.; Oren, A. *Appl. Environ. Microbiol.* **2014**, *80*, 3286 LP–3283295.

(51) de Oliveira, V. E.; Castro, H. V.; Edwards, H. G. M.; de Oliveira, L. F. C. *J. Raman Spectrosc.* **2010**, *41*, 642–650.

(52) Jain, R.; Calderon, D.; Kierski, P. R.; Schurr, M. J.; Czuprynski, C. J.; Murphy, C. J.; McAnulty, J. F.; Abbott, N. L. *Anal. Chem.* **2014**, *86*, 3764–3772.

(53) Bergholt, M.; Serio, A.; Albro, M. *Front. Bioeng. Biotechnol.* **2019**, *7*, No. 303.